Electric Field Modulation of the Membrane Potential in Solid-State Ion Channels

Weihua Guan[†] and Mark A. Reed*,[†],[‡]

[†]Department of Electrical Engineering, Yale University, New Haven, Connecticut 06520, United States
[‡]Department of Applied Physics, Yale University, New Haven, Connecticut 06520, United States

S Supporting Information

ABSTRACT: Biological ion channels are molecular devices that allow a rapid flow of ions across the cell membrane. Normal physiological functions, such as generating action potentials for cell-to-cell communication, are highly dependent on ion channels that can open and close in response to external stimuli for regulating ion permeation. Mimicking these biological functions using synthetic structures is a rapidly progressing yet challenging area. Here we report the electric field modulation of the membrane potential phenomena in mechanically and chemically robust solid-state ion channels, an abiotic analogue to the voltage-gated ion channels in living systems. To understand the complex physicochemical processes in the electric field regulated membrane potential behavior, both quasi-static and transient characteristics of converting transmembrane ion gradients into electric potential are investigated. It is found that the transmembrane potential can be adequately tuned by an external electrical stimulation, thanks to the unique properties of the voltage-regulated selective ion transport through a nanoscale channel.

KEYWORDS: Nanochannel, membrane potential, electrofluidic gating, ion transport, salinity gradient power
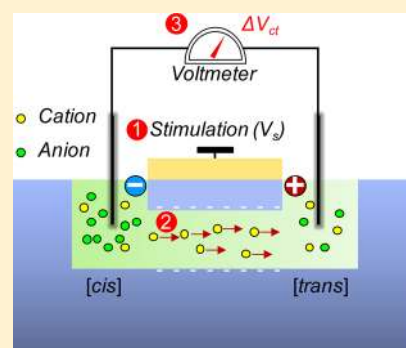
Construction of protocells (artificial cells with a minimum set of components to reproduce one or several cell functions) provides a novel platform to understand the complex biological–physical–chemical processes in a living biological cell. The most indispensable components in constructing protocells are the cell membranes in which ion channels are embedded to facilitate chemical and electrical communication with the extracellular environment. Most of the work so far has used soft materials such as phospholipids and polymersomes to implement the ion channel elements.[1,2] Although these soft materials are native relatives to living cell membranes and have proved to be very useful for a range of interesting experiments,[1] they exhibit a number of disadvantages such as limited stability under various pH, salt concentration, temperature, and mechanical stress conditions. Fabrication of the membranes from solid-state materials presents obvious advantages over their soft matter counterparts, such as very high stability, adjustable surface properties, and the potential for integration into devices and networks. Indeed, development of mechanically and chemically robust solid-state nanopores[2] and nanochannels[3] has already been a rapidly growing area of research due to various practical applications, such as single molecule sensors,[4] energy conversion,[5] and desalination.[6]

One of the most important characteristics in biological ion channels is its selectivity, which allows only specific kind of ions to pass through. The mechanism by which many biological channels achieve selectivity is on the molecular level. For example, in voltage-gated ion channels,[7] a conformational change will be initiated when the proteins bearing charged amino acids inside the ion channel relocates upon changes in the transmembrane electric field. Direct implementing physical conformational variation in solid-state platforms is a daunting task.[8] Instead, the electrostatic interactions, described by Poisson–Nernst–Planck equations,[9–11] are widely used to achieve the charge selectivity in solid-state structures.[12,13]

Inspired by the action potential generation behavior in voltage-gated ion channels, we here propose and demonstrate a solid-state protocell built from top-down fabricated artificial solid-state ion channels (ASIC), whose membrane potential can be modulated by an orthogonal electric field. Previous experimental studies in solid-state nanochannels have considered almost exclusively the voltage-driven phenomena, that is, the passage of ions through the nanochannels upon a potential gradient (i.e., the current–voltage relationship[1,2,12,14]). The membrane potential phenomenon, essentially an open circuit and concentration-driven process, has been barely investigated in artificial ion channel systems.[5,15,16] This study adds another dimension to the unique properties of the regulated selective ion transport through a nanoscale channel.

Device Structures. The protocell we envision to reproduce the membrane potential phenomena in biological cells (Figure 1a) is schematically shown in Figure 1b. It is a three-terminal device that is similar to a nanofluidic field effect transistor
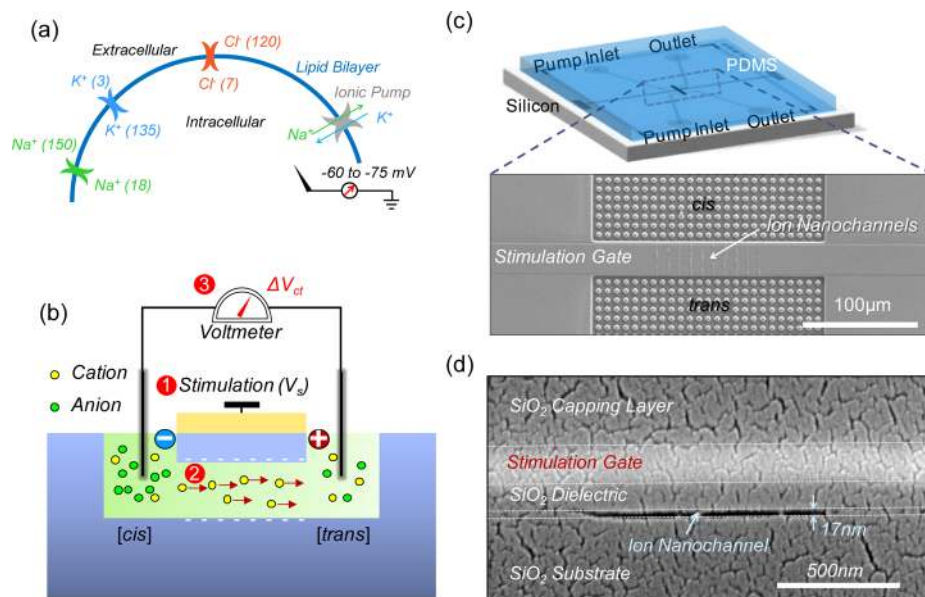
Figure 1. Device principles and experimental setup. (a) Schematic of typical intracellular and extracellular fluid with different ionic concentrations. The cell is in a charge polarization state due to the selective ion transport in ion channels, bringing about a resting membrane potential. (b) Cross-section sketch of the solid-state protocell. A stimulation voltage normal to the nanochannel walls (step 1) alters the ion selectivity in the nanochannel (step 2), resulting in a modulated transmembrane potential (ΔV_{ct}) (step 3). (c) Sketch of the planar layout for the assembled device. Two microfluidic channels pump the electrolyte solutions to the cis and trans reservoirs, formed by SiO_2 trenches with supporting pillars (preventing PDMS collapse), as shown in the magnified scanning electron microscope (SEM) image. (d) Cross-section SEM image showing a single solid-state ion channels with a height of 17 nm and a width of 1 μm.
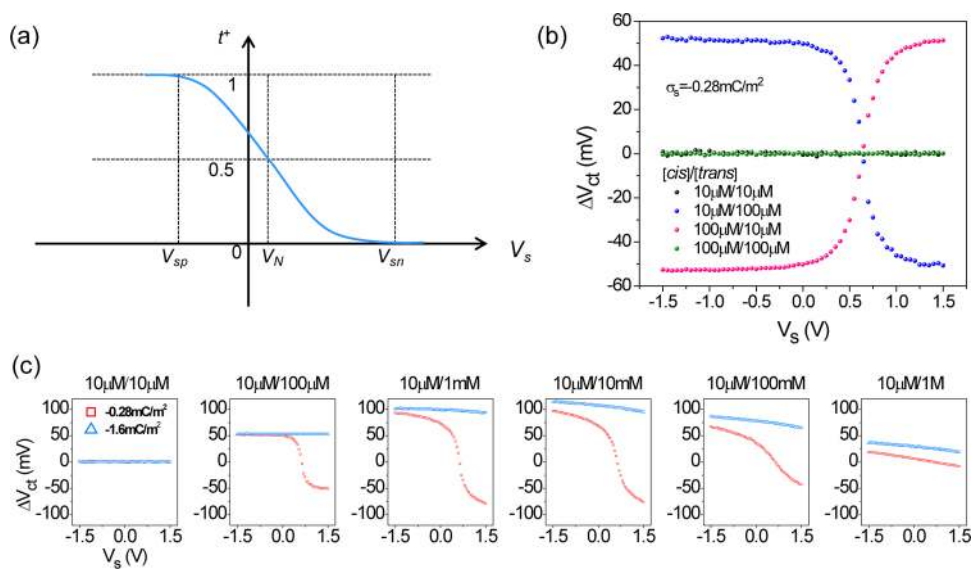

Figure 2. Quasi-static modulation of ΔV_{ct} through stimulation voltage V_s. (a) Cation transport number t^+ as a function of V_s. V_{sp}, V_N, and V_{sn} denote the voltages at which the nanochannel is pure cation selectivity, no selectivity, and pure cation selectivity, respectively. (b) Results in the low salt concentration regime with the device of $\sigma_s = -0.28$ mC/m². Each ΔV_{ct} is recorded 5 s later after applying V_s. (c) Salt concentration dependence of the quasi-static modulation for $\sigma_s = -0.28$ mC/m² (red squares) and for $\sigma_s = -1.6$ mC/m² (blue triangles). The legend denotes [cis]/[trans] conditions. The modulation efficiency ($d\Delta V_{ct}/dV_s$) decreases tremendously in highly charged nanochannels.

(FET),[12,13] except that the longitudinal driving force is a concentration gradient instead of a potential gradient. It is well-known that biological voltage-gated ion channels consist of three basic parts: a voltage sensor, a conducting pathway, and a gate that can physically open/close.[7] The protocell device (Figure 1b) has all of these functional components. The capacitor between the stimulation gate and the nanochannel provides a mechanism for voltage sensing. The electrostatic potential inside the nanochannel forms a virtual potential gate,

regulating the ion permeability through the nanochannel (conducting pathway). The orthogonal electric field, produced by the stimulation voltage (V_s), is expected to mediate the ionic selectivity through electrostatic principles. Standard microprocessing techniques are used to fabricate the protocell devices (Figure 1c). A sacrificial layer removal method with a novel "bond followed by etch" scheme[17] is utilized to reliably produce the nanochannels (ranges from 8 to 20 nm in height, Figure

1d). A detailed description of the device fabrication can be found in the Methods section.

Working Principles. The *steady-state* membrane potential ΔV_{ct} developed across an ion selective membrane (Figure 1b) can be described by,[18]

$$\Delta V_{ct} = (2t^+ - 1)\frac{RT}{F}\ln\frac{[\text{trans}]}{[\text{cis}]} \qquad (1)$$

where R, T, and F are the universal gas constant, absolute temperature, and Faraday constant, respectively. $[x]$ denotes the salt concentration in the x side (x = cis or trans). t^+ is the cation transport number, that is, the ratio of cations to all ions in the channel. With increasing V_s, the cation/anion concentration will be diminished/enhanced accordingly. Therefore t^+ is a monotonic decreasing function of V_s, bounded within 0 and 1 (Figure 2a). The stimulation voltages at which $t^+ \to 1$ (pure cation selectivity), $t^+ = 1/2$ (no selectivity), and $t^+ \to 0$ (pure anion selectivity) is defined as V_{sp}, V_N, and V_{sn}, respectively (Figure 2a). By modulating the steady-state t^+ through stimulation voltage V_s, it is therefore feasible to modulate the membrane potential ΔV_{ct}.

Quasi-Static Behavior. We first carried out quasi-static experiments to verify the above working principles. It is worth noting here that, for the measurement shown in Figure 1b, one cannot ignore that each Ag/AgCl probing electrode is in contact with solutions of different concentrations, and therefore they bear different electrode/electrolyte potentials.[15,19] The measurement gives the potential difference of the whole cell from which the electrode potential difference must be subtracted to obtain the intrinsic ΔV_{ct} value (Supplementary Figure S1). All ΔV_{ct} values presented in this study are after this electrode potential difference correction, unless otherwise noted.

Figure 2b exhibits the steady-state ΔV_{ct} as a function of V_s at low salt concentration conditions, with the device of a reduced surface charge density (σ_s) as -0.28 mC/m² (Supplementary Figure S2). Figure 2b reveals a set of informative features as predicted by eq 1. No membrane potential appears if there is no cis−trans concentration gradient. When $[\text{cis}] < [\text{trans}]$, ΔV_{ct} exhibits the same trend as t^+, while for $[\text{cis}] > [\text{trans}]$, the trend between ΔV_{ct} and t^+ becomes opposite. Moreover, ΔV_{ct} can be modulated into different polarities, thanks to $t^+ > 1/2$ when $V_s = -1.5$ V and $t^+ < 1/2$ when $V_s = 1.5$ V (the V_{sp}, V_N, and V_{sn} value can be extracted from the measurements as -0.15 V, 0.64 V, and 1.25 V, respectively).

The quasi-static ΔV_{ct} modulation is also salt concentration dependent. The red squares in Figure 2c show the steady-state $\Delta V_{ct}-V_s$ relationships for $[\text{trans}]$ ranging from 10 μM to 1 M and $[\text{cis}]$ fixed at 10 μM, using the same device of $\sigma_s = -0.28$ mC/m². As can be seen, when increasing the trans concentration, it is harder and harder to experimentally access the V_{sp} and V_{sn} voltages because of the smaller Debye length compared with the nanochannel dimensions, leading to a situation where creating a unipolar ion environment becomes impossible. The V_N values can be extracted from the $\Delta V_{ct} = 0$ point, which gives the same value of 0.64 V.

Another factor that affects the quasi-static behavior is the surface charge density on the nanochannel walls. The blue triangles in Figure 2c present the results for the device with $\sigma_s = -1.6$ mC/m² (Supplementary Figure S2). With such a high negative surface charge, the nanochannel is dominated by cations ($t^+ > 1/2$), since V_s within $\pm$ 1.5 V is too small to reverse the charge polarity (the smallest absolute V_s required to

reverse is approximately $2\sigma_s d_{ox}/\varepsilon_0\varepsilon_{ox}$, which is around 4.7 V for $\sigma_s = -1.6$ mC/m² and $d_{ox} = 50$ nm). As a result, ΔV_{ct} can only be modulated within the positive range for $[\text{trans}] > [\text{cis}]$ (eq 1). The maximum modulation range of ΔV_{ct} in $\sigma_s = -1.6$ mC/m² is much less than that in $\sigma_s = -0.28$ mC/m², when V_s ranges from -1.5 to 1.5 V. This inefficient modulation is due to the fact that an inherent high surface charge density resembles high densities of surface states in a FET, making electrostatic modulation over the ionic population (and thus t^+) difficult.[17] Therefore, a nanochannel with lower surface charge density is favorable for an efficient modulation of ΔV_{ct}.

A thorough quasi-static $\Delta V_{ct}-V_s$ measurement at various cis and trans concentrations (ranging from 10 μM to 1 M, respectively) is performed for devices with high and low surface charge densities (Supplementary Figure S3). Besides a remarkable qualitative agreement between the experiment and the predictions from eq 1, a reasonable quantitative agreement is also attainable by numerical calculations from both classical Teorell−Meyer−Sievers (TMS) model and space charge (SC) model[20−22] (Supplementary Figure S3).

Transient Behavior. The above quasi-static analysis applies only if the stimulation voltage V_s changes at a rate slower than that required for all ions to redistribute themselves via drift and diffusion. If a voltage ramp is applied, the modulation behavior will depend on the magnitude of dV_s/dt. We investigate here an extreme case with a step V_s to characterize the device transient behavior. A representative ΔV_{ct} waveform as a function of time is shown in Figure 3. The stimulation voltage V_s is stepped from -1.5 to 1.5 V (Figure 3, inset a). Immediately following the applied step, ΔV_{ct} rises from an equilibrium value (state 1) of -69.7 ± 4.40 mV, to a peak value of 452.74 mV, and then decays to another equilibrium value (state 2) of -30.3 ± 4.20 mV with a characteristic relaxation time τ.

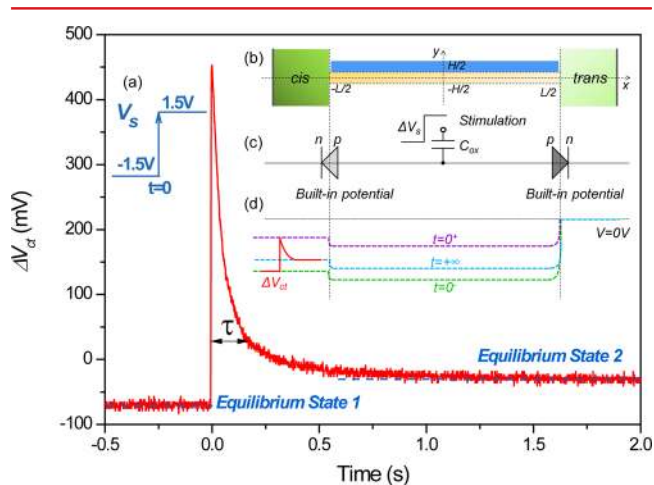**Figure 3.** Transient behavior of ΔV_{ct} upon a step change in the stimulation voltage. Typical transient ΔV_{ct} characteristics when applying a step voltage to the V_s at time $t = 0$. The characteristic relaxation time τ to reach a new equilibrium state can be determined by least-squares exponential fitting. Insets: (a) Schematic of the V_s step. (b) Protocell cross-section with a nanochannel height H and length L. (c) Equivalent circuit of the protocell. (d) Potential profiles in the system at time $t = 0^-$, 0^+, and ∞, respectively. The trans side is grounded. The potential difference in the trans side is much higher than the cis side in this concentration configurations. The time course of ΔV_{ct} is also schematically shown, which qualitatively agrees with the experimental observations.
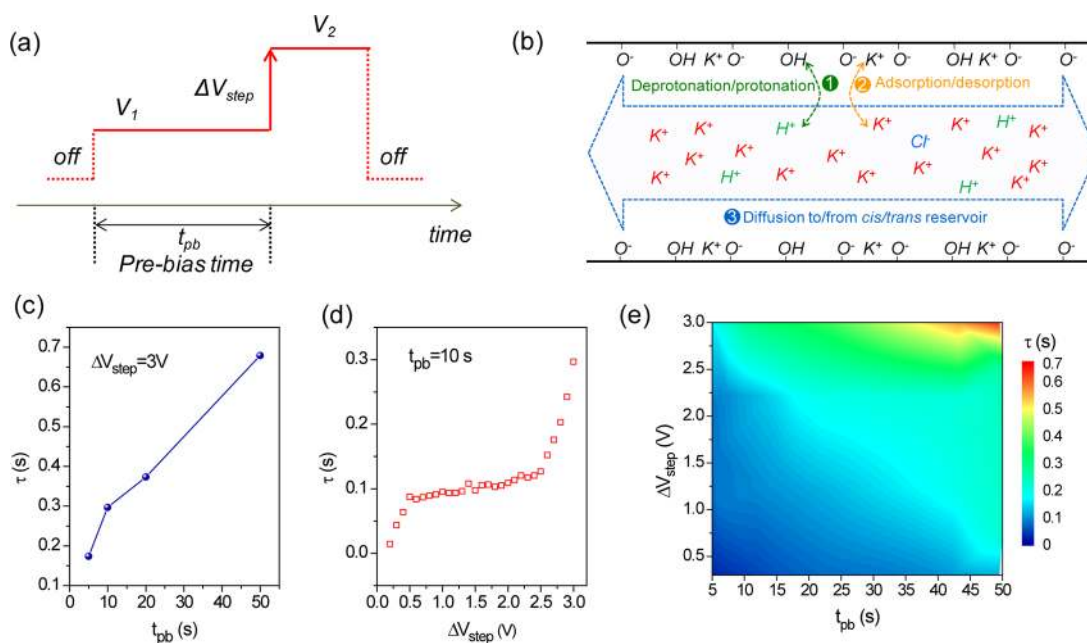
Figure 4. Bias history dependence of the transient characteristic relaxation time. (a) The time sequence of V_s used to test the protocell device. The dashed lines depict no voltage being applied. The device is first biased with voltage V_1 for a period of t_{pb} (prebias time), followed by a sudden change into another level of V_2. (b) Microscopic kinetics during a transient V_s step. (c) The prebias time dependence of the relaxation time under a constant voltage step. (d) The voltage step amplitude dependence of the relaxation time with a fixed prebias time. (e) Contour plot showing the relaxation time as a function of both the prebias time and the voltage step amplitude.

The variation of ΔV_{ct} following a step in stimulation voltage V_s can be understood by looking at the device structure (Figure 3, inset b) and its equivalent circuit (Figure 3, inset c). A micro/nano channel interface acts as an ionic diode, with a cation selective nanochannel as a p region.[14] Therefore, the two micro/nano channel interfaces can be treated as two diodes,[23] connecting anode-to-anode through the nanochannel, capacitively coupled to the stimulation electrode through a capacitor C_{ox} (Figure 3, inset c). Let us now consider one of the diodes. When a charge-selective nanochannel is in isothermal Donnan equilibrium with an adjacent microfluidic reservoir, a Donnan potential will appear at the micro/nano channel interface and can be expressed as[24] $V_D = (RT/z_iF)\ln(c_i^{nc}/c_i^{bulk})$, where z_i is the valence of ion i and c_i^{nc} and c_i^{bulk} are the concentration of ion i in the nanochannel and in the reservoir, respectively. This Donnan potential is analogous to the built-in potential in semiconductor diodes. It can be seen that the higher the reservoir concentration, the lower the Donnan potential. For the case of [cis]/[trans] = 100 mM/100 μM, the Donnan potential in the trans side is much higher than the cis side.

Referring to the inset d of Figure 3, immediately after the V_s step is applied ($t = 0^+$), the floating nanochannel body potential will exactly follow the rapid change in V_s (dashed purple line). As a result, ΔV_{ct} will experience the same abrupt change as in V_s, up to the amount allowed by RC time constant limitations (i.e., ΔV_{ct} at $t = 0^+$ (~ 0.5 V) is less than the step change in V_s (3 V)). Following this, the potentials in the system will attempt to reach steady-state as ions redistribute themselves via Poisson−Nernst−Planck principles[10,11,25] (dashed blue line). This equivalent picture thus successfully explains the observed time evolution of ΔV_{ct}. For completeness, notice that a falling edge step in V_s, shows a similar but inverted behavior (Supplementary Figure S4).

Identifying Factors Affecting Characteristic Relaxation Time. When applying an abrupt step stimulation voltage

(Figure 4a), the ionic concentration and potential distribution in the nanochannel is disturbed from equilibrium. In a hydroxyl group terminated SiO_2 nanochannel filled with KCl solution, there are three possible physicochemical processes happening during this transient period[26] (Figure 4b): (1) protonation or deprotonation upon external electric field, (2) adsorption or desorption of counterions in the Stern layer, and (3) ion exchange between the nanochannel and reservoirs. These three dynamic processes taken together determine the characteristic time required to reach a new equilibrium.

Processes 1 and 2 are channel surface-related radial dynamics that are dependent on the bias history of V_s. We found in the experiments that the characteristic relaxation time τ is dependent on both the prebias time (t_{pb}) and the step amplitude (ΔV_{step}) of V_s (Figure 4a). With a fixed voltage step, the longer the prebias time, the slower it is to reach a new equilibrium (Figure 4c), while for a fixed prebias time, a larger step voltage in V_s results in a larger τ value (Figure 4d). Figure 4e further shows the characteristic relaxation time is indeed affected by both t_{pb} and ΔV_{step}. This dependence of τ on the V_s history is because the amount of the transiently generated/diminished H^+ or K^+ is strongly affected by the prebias time and the voltage step amplitude. For example, Eijkel et al. showed that the capacitive release or uptake of protons at the dielectric-electrolyte interface is positively proportional to the applied voltage,[27] whereas Han et al. showed that the small but inevitable leakage current related water electrolysis produces a change of proton concentration, affected by both the bias voltage and time.[28] An excessive amount of the transient ions requires a longer time to remove before reaching another equilibrium state. It is thus important that any valid comparison on the relaxation time must be performed with the same bias history to ensure a comparable starting microenvironment.

Process 3 is an axial kinetic process which is governed by the ambipolar drift-diffusion equation without generation and
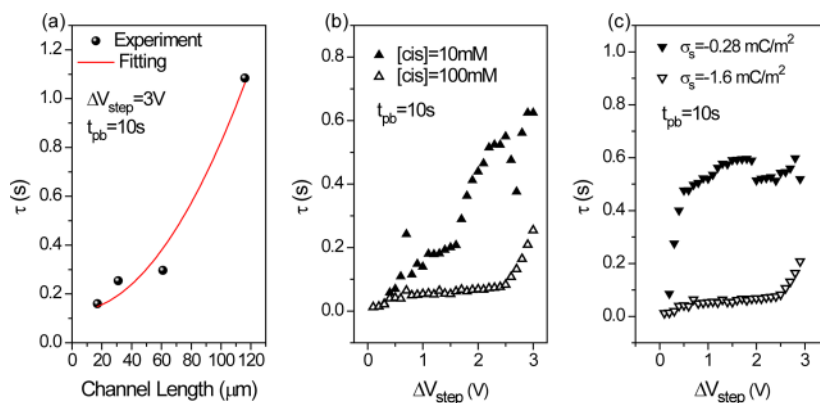
Figure 5. Device parameter dependence of the characteristic relaxation time. (a) Nanochannel length dependence. The solid line shows a parabolic fitting of the relaxation time as a function of nanochannel length. (b) Microfluidic reservoir concentration dependence. The trans side is fixed with 100 μM KCl. The test is done with a device of channel length $L = 31$ μm and $\sigma_s = -1.6$ mC/m^2. (c) Surface charge density dependence. The test is carried out on the same device before and after the surface chemical modification, with $L = 61$ μm and [cis]/[trans] = 100 mM/100 μM.

recombination.[12] The characteristic time in this process can be estimated as $\tau \sim L^2/4D_a$, where L is the diffusion length and D_a is the ambipolar diffusion coefficient (Supplementary Methods). Figure 5a shows the characteristic time as a function of nanochannel length ranging from 17 to 116 μm, with ΔV_{step} and t_{pb} being constant (decoupling the axial process from the radial process to make the comparison valid). The parabolic fitting curve in Figure 5a demonstrates a remarkable agreement with the predicted parabolic dependence of τ on the channel length.

The axial kinetics (process 3) are also dependent on the reservoir concentrations. We measured the characteristic time for different salt concentrations. As shown in Figure 5b, the case of [cis] = 100 mM takes less time to reach equilibrium than the case of [cis] = 10 mM at a same ΔV_{step} (both with [trans] = 100 μM). This reduced τ value at higher cis concentration is because of two factors. First, the higher the cis concentration, the more pronounced Debye screening in the cis side of the nanochannel. The effective channel length is therefore reduced in the [cis] = 100 mM case, resulting in a short diffusion time. Second, the relative change of the ion concentration in the [cis] = 100 mM case is much smaller than in the [cis] = 10 mM case (Supplementary Figure S5). As a result, less time is needed to reach a new equilibrium in the high concentration case. Figure 5b also shows the slope of the $\tau \sim \Delta V_{step}$ is dependent on the salt concentrations. This can be explained by the model proposed by Eijkel et al.,[27] where the amount of protons transiently generated upon an applied gate voltage can be expressed as $N = V_S C_{ox} C_{buff}/(C_{buff} + C_{DL})$, in which C_{buff} is the surface intrinsic (chemical) buffer capacitance and C_{DL} is the double layer capacitance. As a result, $d\tau/dV_S \sim dN/dV_S \sim 1/(C_{buff} + C_{DL})$. Increasing the salt concentration will lead to an increase of C_{DL} and thus a decreased $d\tau/dV_S$, consistent with Figure 5b.

We also investigate the effect of nanochannel surface charge density on the characteristic time. Figure 5c shows that it takes longer time for the low surface charge density device (with $\sigma_s = -0.28$ mC/m^2) to reach a new equilibrium than the native device (with $\sigma_s = -1.6$ mC/m^2). This can also be understood by looking at the relative ion concentration change in the nanochannel. With a reduced σ_s, a larger relative concentration change occurs because of the more effective ion population modulation. A numerical calculation shows that the relative concentration change is indeed higher in the nanochannel with

a less charged surface (Supplementary Figure S6). The slope of the $\tau \sim \Delta V_{step}$ is less dependent on the surface charge densities at intermediate ΔV_{step}, as expected by $d\tau/dV_S \sim 1/(C_{buff} + C_{DL})$. This result, combined with the data shown in Figure 2, indicates that there is a trade-off between the stimulation efficiency and speed, owing to the surface charge effect.

Frequency-Dependent Switching Behavior. The step analysis suggests the maximum continuous operation speed for the protocell device. The dynamic behavior of the protocell in continuous operation must be frequency-dependent. Once the ASIC is disturbed from steady-state, the ability to reach a new equilibrium before the next clock cycle is determined by the switching period. Increasing frequency will produce less changes in ionic concentrations from one cycle to the other, since the radial surface reaction and the axial drift-diffusion do not have enough time to respond. Therefore, it can be expected that the modulation of the *ion-contributed* ΔV_{ct} will disappear at high frequencies. Figure 6 shows the ΔV_{ct} waveforms in continuous switching operations under various frequencies. At lower frequencies (10 mHz to 1 Hz), ΔV_{ct} can always be modulated stably between two steady-state values (indicated by two arrows, -31 mV and -43 mV). At higher frequencies (>1 Hz), each clock-cycle is too short for the system to reach an ionic equilibrium, and therefore the membrane potential ΔV_{ct} value cannot be modulated between two steady-state values. The modulation of ΔV_{ct} at higher frequencies mostly comes from the electronic contributions instead of ionic ones, owing to the close coupling of the floating nanochannel body potential to V_s at the rising or falling edges (Figure 3c). These results indicate a protocell device of maximum operation frequency around 1 Hz, which can be further increased toward the maximum action potential frequency in biological nerve cells (~200 Hz) by shrinking the device length (i.e., adopting a gated nanopore structure[29]) and tailoring the surface charges.

Conclusions. In conclusion, we have demonstrated a solid-state protocell with engineered ion channels, whose ion selectivity and membrane potential can be modulated by external electric field, harvesting the major components in a biological voltage-gated ion channel. It can also be viewed as a universal ion exchange membrane,[30] where similar membrane potential modulation has been observed. The experimental results on quasi-statically converting the transmembrane ion gradients into potential validate the voltage regulated selectivity mechanism. Critical factors that affect the modulation efficiency
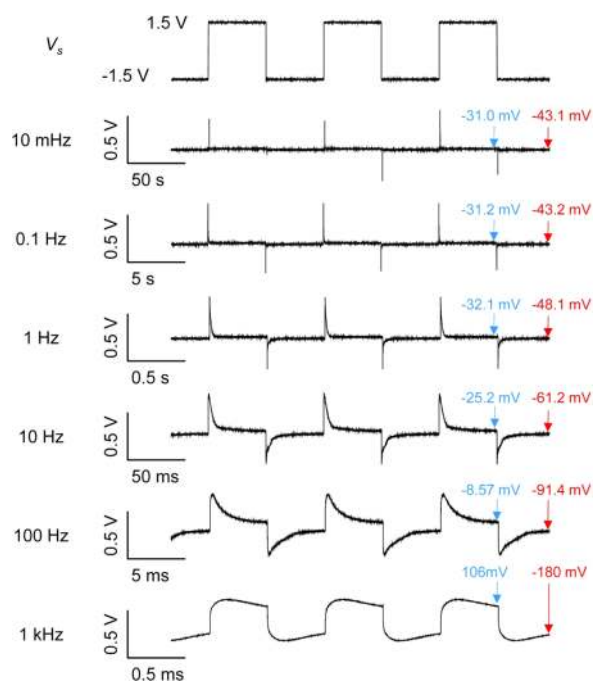
Figure 6. Frequency dependence of the continuous switching behavior. The stimulation voltage is switched back-and-forth between −1.5 and 1.5 V (first row). The corresponding ΔV_{ct} waveform shows a strong dependence on the operation frequency. The dashed green and solid red arrows denote the potential value right before the falling edge and the rising edge, respectively. This test indicates a maximum operation frequency around 1 Hz for this particular device ($L = 17\ \mu m$, $\sigma_s = -1.8\ mC/m^2$, and [cis]/[trans] = 100 mM/100 μM).

and transient modulation speed are also identified, which has an immediate indication to the transient performances in nano-fluidic FETs[12,26] and chemical charge coupled devices.[31] As a concentration-driven system, the top-down fabricated solid-state protocells provide an excellent engineered model platform to study the membrane phenomena in biological samples, which would lead to the creation of engineered nerve cells and neuron networks due to this approach's potential of integration and surface tailoring. It also has practical indications to desalination and energy generation using solid-state structures.

Methods. *Device Fabrication.* We used a sacrificial layer method, more specifically, a "bond followed by etch" scheme, to produce the nanochannels.[17] Starting with a 4 in. SiO$_2$/Si wafer, an array of chromium thin films are patterned by wet etching. A dielectric SiO$_2$ layer is then deposited by plasma enhanced chemical vapor deposition and followed by a rapid thermal annealing process to improve its quality. A stimulation gate electrode is thereafter formed by a double layer lift-off process. The reservoirs with supporting pillars and the gate electrode bonding pad are etched simultaneously by reactive CHF$_3$/Ar plasma. The device is then aligned and permanently bonded with a microfluidic polydimethylsiloxane stamp by treating them with oxygen plasma. The Cr etchant is pumped into the microchannel and diffusively etches the Cr sacrificial layer in situ. The end-point detection for the etching process is done by looking at the color contrast under a microscope. Deionized water is flushed through the microchannel to rinse the device after the etching process is over, and then the device is ready to use.

Electrical Characterization. The whole testing procedure is done using an automatic system. The solutions were delivered at a constant flow rate of 2 $\mu L/min$ by pumps (New Era Pump Systems), controlled by a LabVIEW (National Instruments) program. The nanochannels were pumped with deionized water for at least 3 h before use. Aqueous KCl solution is used as a testing electrolyte. The electrical contacts are made of Ag/AgCl electrodes. The quasi-static test is stimulated and measured using two Keithley 2400 sourcemeters. The transient behavior is stimulated and measured by Tektronix AFG 3252 and DPO 4104, respectively. Data postprocessing is done with MATLAB (The MathWorks) software. All measurements are performed inside a Faraday cage at room temperature (298 K).

Numerical Calculation. The steady-state distributions of the cation/anion concentration and the open circuit potential are calculated by solving the coupled 2D Poisson−Nernst−Planck (PNP) equations in COMSOL script environment. We use three modules in the COMSOL environment: electrostatics (AC/DC Module), Nernst−Planck without electroneutrality for the calculation of K$^+$ ions (Chemical Engineering Module), and Nernst−Planck without electroneutrality for the calculation of Cl$^-$ ions (Chemical Engineering Module). The simulation system contains a 20-nm-high nanochannel with different physically measured lengths, connected by two 10 × 10 μm^2 square reservoirs with various bath concentrations.

■ ASSOCIATED CONTENT

Ⓢ Supporting Information
Details of electrode potential difference correction, surface charge measurement and modification procedure, and numerical calculations. This material is available free of charge via the Internet at http://pubs.acs.org.

■ AUTHOR INFORMATION

Corresponding Author
*E-mail: mark.reed@yale.edu.
Notes
The authors declare no competing financial interest.

■ ACKNOWLEDGMENTS

■ REFERENCES

(1) Maglia, G.; Heron, A. J.; Hwang, W. L.; Holden, M. A.; Mikhailova, E.; Li, Q. H.; Cheley, S.; Bayley, H. *Nat. Nanotechnol.* **2009**, *4*, 437−440.
(2) Dekker, C. *Nat. Nanotechnol.* **2007**, *2*, 209−215.
(3) Duan, C. H.; Majumdar, A. *Nat. Nanotechnol.* **2010**, *5*, 848−852.
(4) Wei, R. S.; Gatterdam, V.; Wieneke, R.; Tampe, R.; Rant, U. *Nat. Nanotechnol.* **2012**, *7*, 257−263.
(5) Guo, W.; Cao, L. X.; Xia, J. C.; Nie, F. Q.; Ma, W.; Xue, J. M.; Song, Y. L.; Zhu, D. B.; Wang, Y. G.; Jiang, L. *Adv. Funct. Mater.* **2010**, *20*, 1339−1344.

(6) Kim, S. J.; Ko, S. H.; Kang, K. H.; Han, J. *Nat. Nanotechnol.* **2010**, *5*, 297−301.

(7) Bezanilla, F. *IEEE Trans. NanoBiosci.* **2005**, *4*, 34−48.

(8) Siwy, Z. S.; Howorka, S. *Chem. Soc. Rev.* **2010**, *39*, 1115−1132.

(9) Chen, D.; Lear, J.; Eisenberg, B. *Biophys. J.* **1997**, *72*, 97−116.

(10) Daiguji, H.; Yang, P. D.; Majumdar, A. *Nano Lett.* **2004**, *4*, 137−142.

(11) Vlassiouk, I.; Smirnov, S.; Siwy, Z. *Nano Lett.* **2008**, *8*, 1978−1985.

(12) Gajar, S. A.; Geis, M. W. *J. Electrochem. Soc.* **1992**, *139*, 2833−2840.

(13) Karnik, R.; Fan, R.; Yue, M.; Li, D. Y.; Yang, P. D.; Majumdar, A. *Nano Lett.* **2005**, *5*, 943−948.

(14) Gijs, M. A. M. *Nat. Nanotechnol.* **2007**, *2*, 268−270.

(15) Xu, J.; Sigworth, F. J.; LaVan, D. A. *Adv. Mater.* **2010**, *22*, 120−127.

(16) Kim, D. K.; Duan, C. H.; Chen, Y. F.; Majumdar, A. *Microfluid. Nanofluid.* **2010**, *9*, 1215−1224.

(17) Guan, W. H.; Fan, R.; Reed, M. A. *Nat. Commun.* **2011**, *2*, 506.

(18) Lakshminarayanaiah, N. *Equations of Membrane Biophysics*; Academic Press: New York, 1984.

(19) Helfferich, F. *Ion Exchange*; McGraw-Hill Book Company: New York, 1962.

(20) Westermannclark, G. B.; Christoforou, C. C. *J. Electroanal. Chem.* **1986**, *198*, 213−231.

(21) Zambrowicz, E. B.; Colombini, M. *Biophys. J.* **1993**, *65*, 1093−1100.

(22) Wang, X. L.; Tsuru, T.; Nakao, S.; Kimura, S. *J. Membr. Sci.* **1995**, *103*, 117−133.

(23) Cheng, L. J.; Guo, L. J. *Microfluid. Nanofluid.* **2010**, *9*, 1033−1039.

(24) Schoch, R. B.; Han, J. Y.; Renaud, P. *Rev. Mod. Phys.* **2008**, *80*, 839−883.

(25) Constantin, D.; Siwy, Z. S. *Phys. Rev. E* **2007**, *76*, 041202.

(26) Fan, R.; Yue, M.; Karnik, R.; Majumdar, A.; Yang, P. D. *Phys. Rev. Lett.* **2005**, *95*, 086607.

(27) Veenhuis, R. B. H.; van der Wouden, E. J.; van Nieuwkasteele, J. W.; van den Berg, A.; Eijkel, J. C. T. *Lab Chip* **2009**, *9*, 3472−3480.

(28) Oh, Y. J.; Bottenus, D.; Ivory, C. F.; Han, S. M. *Lab Chip* **2009**, *9*, 1609−1617.

(29) Nam, S. W.; Rooks, M. J.; Kim, K. B.; Rossnagel, S. M. *Nano Lett.* **2009**, *9*, 2044−2048.

(30) Nishizawa, M.; Menon, V. P.; Martin, C. R. *Science* **1995**, *268*, 700−702.

(31) Stern, M. B.; Geis, M. W.; Curtin, J. E. *J. Vac. Sci. Technol. B* **1997**, *15*, 2887−2891.